Research Square

Preprints are preliminary reports that have not undergone peer review.
They should not be considered conclusive, used to inform clinical practice,
or referenced by the media as validated information.

Phase Evolution and Nanostructural Properties of Tungsten Carbide Coatings Fabricated via Methane-Assisted Dense Plasma Focus Discharges

Noushin Yasavol

nyasavol@aeoi.org.ir

Amir Raeisdana

Research Article

Keywords: Plasma-Facing Components, Tungsten Carbide, Nanocrystalline, Plasma Focus

Posted Date: November 24th, 2026

DOI: https://doi.org/10.21203/rs.3.rs-11589074/v1

License: This work is licensed under a Creative Commons Attribution 4.0 International License.
Read Full License

Additional Declarations: No competing interests reported.

Phase Evolution and Nanostructural Properties of Tungsten Carbide Coatings Fabricated via Methane-Assisted Dense Plasma Focus Discharges

N. Yasavol*, A. Raeisdana

Plasma and Nuclear Fusion Research School, Nuclear Science and Technology Research Institute (NSTRI) Atomic Energy Organization of Iran, Tehran, Iran,
nyasavol@aeoi.org.ir

Abstract:

This study investigates the synthesis and microstructural evolution of nanostructured tungsten carbide coatings on tungsten substrates utilizing pulsed dense plasma focus (DPF) discharges under methane working gas. Benefiting from the short pulse duration and the high thermal conductivity of the underlying tungsten substrate (~170 W/m·K), the melted surface layer experiences ultra-fast quenching (10^7–10^9 K/s), effectively arresting grain growth within the nanocrystalline regime (18–32 nm). X-ray diffraction (XRD) reveals a clear phase transition governed by the shot count and carbon flux: a 60-shot discharge with a graphite-installed anode traps the non-equilibrium, sub-stoichiometric hemitungsten carbide (W_2C) phase alongside WC. Increasing irradiation to 70 shots drives complete carburization, yielding a single-phase, highly crystalline α-WC coating. At 90 shots, the stoichiometric WC matrix is retained, accompanied by pronounced diffraction peak broadening and defect-induced lattice strain. Scanning electron microscopy (SEM) demonstrates a hierarchical surface morphology formed by non-equilibrium solidification, transitioning from partially melted, crater-like features at 60 shots to dense arrays of spherical nanoparticles and shockwave-induced micro-droplets (1–3 μm) at 70 shots. These findings demonstrate that single-step methane-assisted DPF surface carburization provides an effective, non-equilibrium processing route for tailoring phase composition and nanocrystalline architecture in tungsten-based plasma-facing materials without requiring post-deposition heat treatments.

Key word: Plasma-Facing Components; Tungsten Carbide; Nanocrystalline; Plasma Focus;

1. Introduction

The selection and optimization of plasma-facing materials (PFMs) for the divertor armor and first-wall structures of magnetic confinement fusion devices, such as ITER and DEMO, constitute one of the most critical engineering challenges in advanced nuclear

energy systems [1, 2]. Tungsten (W) is currently considered the primary candidate material for these components owing to its exceptionally high melting temperature (3422 °C), elevated thermal conductivity, low physical sputtering yield under light-ion bombardment, and low tritium inventory retention under steady-state operating regimes [3, 4].

Despite these favorable bulk properties, monolithic tungsten is subject to severe structural degradation under extreme transient heat fluxes and off-normal plasma events, including Edge Localized Modes (ELMs) and vertical displacement events (disruptions) [5, 6]. These high-heat-flux transient spikes—often reaching peak power densities between 0.5 and 2.0 GW/m^2 on sub-millisecond timescales—exceed the thermal shock threshold of tungsten, causing localized surface melting, droplet splashing, and rapid recrystallization above 1200–1300 °C [6, 7]. Recrystallization induces grain coarsening and drives the material into ductile-to-brittle transition temperature (DBTT) embrittlement, resulting in extensive thermal fatigue micro-cracking, surface blistering from helium/hydrogen irradiation, and substantial dust mobilization within the plasma chamber [8, 9].

To mitigate these degradation phenomena without compromising the core thermal dissipation capability of the underlying bulk metal, surface engineering through the in-situ synthesis of refractory tungsten carbide (WC/ W_2C) nanocomposite layers presents an attractive strategy [10, 11]. Nanostructured tungsten carbide ceramics exhibit superior mechanical hardness, high thermodynamic stability, elevated cohesive surface binding energy, and high resistance to physical/chemical erosion under reactive plasma environments [12, 13]. Furthermore, ultra-fine nanocrystalline grain boundaries serve as effective neutral sinks for radiation-induced point defects, thereby suppressing helium bubble coalescence and subsurface blistering [14].

Among various energetic transient plasma surface treatment technologies, the Mather-type Dense Plasma Focus (DPF) device provides a highly non-equilibrium processing environment [15, 16]. The DPF discharge produces high-energy ion beams, relativistic electron streams, and supersonic dense plasma fountains with rapid thermal quenching rates on the order of 10^7 to 10^9 K/s [17, 18]. Operating the DPF in a pure methane (CH_4) atmosphere combined with a carbon/graphite anode insert facilitates simultaneous ion implantation, precursor gas dissociation, and transient surface melting, culminating in the rapid non-equilibrium crystallization of ultra-fine tungsten carbide phases without requiring high-temperature post-annealing treatments [19, 20].

In the present study, nanostructured tungsten carbide (WC/ W_2C) composite surface layers were synthesized on pure polycrystalline tungsten substrates using a 115-kJ inverted Mather-type DPF facility (IR-MPF-100) operating with pure methane filling gas and a graphite -inserted anode tip. The phase evolution, crystallite size, lattice microstrain, surface topography, elemental composition, and apparent contact microhardness were systematically evaluated using X-ray diffraction (XRD), field emission scanning electron microscopy (FE-SEM), atomic force microscopy (AFM), CHNS elemental analysis, and Vickers micro-indentation. The fundamental 4-stage plasma synthesis mechanism and the

mechanical load-bearing behavior of the modified surface layers are discussed in detail in the context of plasma-facing component requirements.

2. Experimental Details

The deposition and synthesis processes were conducted using a 115 kJ Mather-type Dense Plasma Focus (DPF) device (IR-MPF-100). As illustrated in Figure 1, the device features a specific inverted geometry where the anode and cathode are oriented in a downward position. This configuration is essential for the process, as it facilitates the direct projection and rapid solidification of anode-ablated material onto the substrate. The process is driven by intense plasma shock waves and high-energy ion bombardment, which ensures the formation of coatings with superior metallurgical adhesion.

The depositions were carried out under three distinct reactive environments and operational conditions: Methane gas with a graphite target (60 shots). Pure methane gas (70 shots). Methane gas with a graphite target (90 shots). Following the deposition, the characterization of the samples was performed through the following techniques:

Phase Identification: The crystal structure and phase composition were analyzed using X-ray Diffraction (XRD) with Cu-K alpha radiation (wavelength 1.5406 Angstroms).
Morphological Analysis: Surface and cross-sectional features were examined using a Zeiss Field Emission Scanning Electron Microscope (FE-SEM) operating at an accelerating voltage of 20 kV.

Topography Evaluation: Surface roughness and height profiles were measured using contact-mode Atomic Force Microscopy (AFM).

Elemental Analysis: The carbon content incorporated into the tungsten lattice were quantified using a CHNOS elemental analyzer.

Mechanical Properties: The micro-hardness of the coatings was evaluated using a Micro-Vickers hardness tester with a 300-gf load (HV0.3). Measurements were taken at 3 multiple locations across the surface to confirm the uniformity of the coating layer.

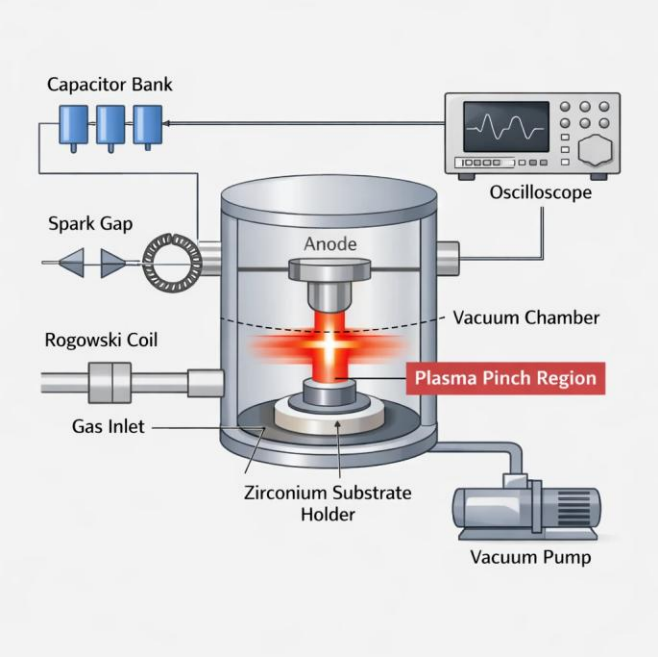


Figure 1: Schematic of the IR-MPF-100 plasma focus device. Installation of graphite in the anode head area and placement of the tungsten substrate at a distance of 35cm away from the anode head.

3. Results and Discussion

3.1. X-ray Diffraction (XRD) Analysis and Structural Evolution

The crystallographic evolution, phase identification, and microstructure of the modified tungsten substrates processed under pure methane (CH_4) working gas environments, varying discharge dosages (60, 70, and 90 shots), and different anode tip configurations were systematically evaluated XRD according to Figure 2. In this investigation, "CH_4" corresponds to discharges performed with a conventional anode tip, while "CH_4 + G" indicates the implementation of a graphite-modified central anode tip. Figure 2 displays the recorded XRD patterns for the three experimental conditions: a) 60 shots +G, b) 70 shots, and c) 90 shots + G.

3.1.1. Role of the Graphite-Modified Anode Tip (G)

The insertion of a graphite disk at the anode tip radically alters the plasma-material interaction and species ablation dynamics during the radial pinch phase. In typical Mather-type DPF configurations, extreme pinch currents and intense transient thermal fluxes induce rapid ablation of the anode material [16, 18]. When a graphite-enhanced tip is deployed: The ablated flux contains not only tungsten atomic species and ionized clusters, but also an abundant supply of energetic atomic carbon and high-reactivity hydrocarbon radicals arising from the explosive thermal exfoliation of graphite sheets [21, 22]. This

solid-state carbon ablation acts in synergy with the gaseous methane atmosphere, substantially raising the local carbon chemical potential within the expanding plasma jet [23, 24]. Consequently, while the standard CH_4 discharges predominantly promote the growth of stoichiometric alpha-WC phases, the CH_4 + G configuration at 60 shots facilitates the formation of mixed carbide structures, including hexagonal W_2C and intermediate sub-carbide phases, as evidenced by the distinct diffraction features near $2\theta \sim 53.5$ deg and 73.2 deg. This multi-phase carbide evolution aligns with observations reported by Rawat et al. [18] and Niranjan et al. [25], who emphasized that elevated carbon flux density during pulsed pinch impacts promotes continuous phase transitions and non-equilibrium carbide nucleation.

3.1.2. Influence of Methane Working Gas and Carburization Mechanisms

The methane ambient gas functions as an active precursor for in-situ carbon transport during both the axial run-down and pinch phases: For pure CH_4 discharges (60 and 70 shots, standard anode), the diffraction profiles exhibit a pronounced, narrow Bragg reflection at $2\theta \sim 33.5$ deg, corresponding to the (100) plane of hexagonal tungsten carbide (alpha-WC, JCPDS card no. 51-0939), alongside lower intensity reflections corresponding to the (101) and (110) planes at $2\theta \sim 48.2$ deg and 68.4 deg [11, 26]. The intense (100) reflection observed in the 70-shot specimen indicates a strong preferential crystallographic orientation and high degree of crystallinity. As the high-temperature plasma sheath collides with the substrate surface, continuous dissociation of CH_4 molecules into energetic C^+, H^+, and CH_x radicals takes place [18, 27].

The simultaneous deposition of energetic carbon ions and intense local heating causes instantaneous melting of the outermost tungsten layer, followed by rapid liquid-state diffusion and epitaxial-like re-solidification [28, 29]. These findings are in strong agreement with Momen-Baghdadabad et al. [30] and Akel et al. [31], who reported that moderate methane ion beam bombardment promotes preferential textured growth along lower surface energy planes without undesirable oxide formation.

3.1.3. Impact of Cumulative Discharge Dosages (60, 70, vs. 90 Shots)

Varying the cumulative shot number from 60 to 70 and subsequently to 90 shots profoundly alters the thermal accumulation, lattice strain, and dislocation density within the modified zone: At 60 shots, initial carbide nucleation begins, but the lower cumulative energy deposition yields broader peaks with moderate diffraction intensity. Elevating the dosage to 70 shots achieves an optimal balance between energy deposition, atomic diffusion, and grain coalescence, resulting in sharp, well-defined diffraction peaks indicative of stress relaxation and superior grain ordering [26, 32]. At 90 shots (combined with the graphite tip), a significant shift in the primary diffraction angle toward higher 2θ values (~53.5 deg) is clearly observed. This angular displacement and associated peak broadening are driven by two main mechanisms: 1) Cumulative thermal shock cycles:

Repeated high-flux plasma impacts subject the surface to severe thermal stress and ultra-fast cooling rates (exceeding 10^7 K/s), inducing high densities of crystalline defects, stacking faults, and dislocation networks [33, 34]. 2) Interstitial super-saturation and macro-compressive stress: Repetitive energetic ion implantation (peening effect) drives surplus carbon atoms into octahedral interstitial sites of the tungsten lattice, causing extensive lattice distortion, unit cell contraction, and significant residual compressive stress [35, 36]. Similar peak shift phenomena toward higher diffraction angles under cumulative DPF shot numbers have been extensively documented by Zandrahimi and Bakhshi [37] as well as Hassan et al. [38] for pulsed plasma treated transition metals.

The appearance of distinct reflections at $2\theta \approx 58°$ and 73° in the 60-shot sample indicates the formation of the sub-stoichiometric W_2C phase, confirming a mixed WC/ W_2C matrix [25]. However, as the discharge dosage increases to 70 and 90 shots, these reflections vanish, leaving only the stoichiometric WC phase. This complete transition is attributed to the sustained and higher cumulative carbon flux, which facilitates full carburization of the coating [25, 31].

In conclusion, standard Z-discharges at 60 shots result in a mixed WC/ W_2C carbide matrix. Increasing the discharge to 70 shots promotes a transition toward a highly oriented, crystalline α-WC coating. Furthermore, the combination of a graphite-modified anode and 90 shots (CH_4 + G) produces a dense, multi-phase WC surface layer characterized by significant defect-induced lattice strain and residual compressive stress.

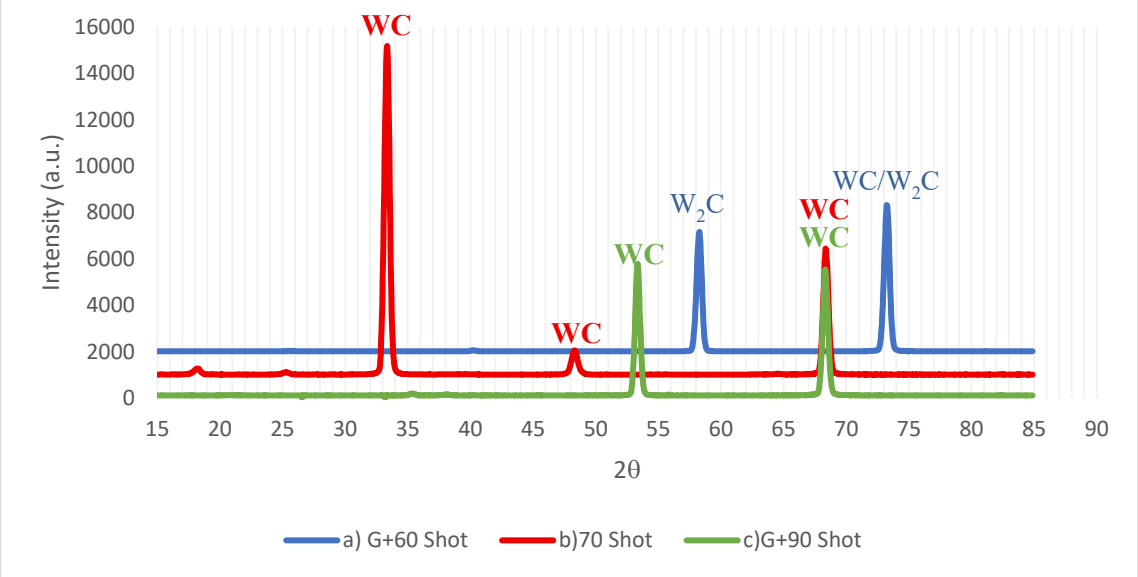


Figure 2: X-ray diffraction (XRD) patterns of tungsten substrates treated under different plasma focus discharge conditions. The curves represent: (a) 60 shots in a pure CH_4 environment, (b) 70 shots in a pure CH_4 environment, and (c) 90 shots in a pure CH_4 environment utilizing a graphite-modified anode tip (G). The diffraction peaks indicate the formation of hexagonal tungsten carbide (α-WC) and the evolution of the W_2C phase in the high-dosage graphite-assisted sample.

3.1.4 Quantitative X-ray Diffraction and Microstructural Analysis

To gain deeper quantitative insight into the microstructural evolution and grain refinement induced by the DPF treatment, peak profile analysis was conducted on the prominent diffraction peaks of the treated tungsten substrate and the newly formed tungsten carbide phases.

The structural parameters, crystallographic planes, and corresponding full-width at half-maximum (FWHM) characteristics derived from the XRD patterns are summarized in Table 1. The peak broadening exhibits a non-monotonic behavior as a function of plasma dosage. The G+60 shot sample displays the broadest reflections, which corresponds to the coexistence of the intermediate W_2C phase and incomplete lattice ordering. Upon increasing to 70 shots, a prominent narrowing of the reflections is observed, indicating an optimal crystallite coherence length (28–32 nm) and the complete formation of single-phase α-WC. Conversely, extended exposure to 90 shots leads to a noticeable re-broadening of the α-WC peaks, which is attributed to severe defect-induced micro-strain and plasma shockwave-induced lattice distortion rather than phase separation.

Table 1: XRD structural parameters, diffraction plane assignments, and relative FWHM evolution for DPF-treated tungsten under different shot dosages.

Sample ID	Discharge Condition	Identified Phase	Assigned Plane (hkl)	Approx. 2θ (deg)	FWHM Trend	Crystallite Size & Characteristics
G + 60 Shots	Graphite tip, 60 shots	W, alpha-WC, W_2C	(110), (100), (102), (110)	40.3, 35.6, 58.0, 73.0	Broadest	~18–20 nm; Multi-phase, incomplete carburization.
70 Shots	Standard, 70 shots	alpha-WC	(001), (100), (110), (101)	31.5, 35.6, 40.3, 48.3	Narrowest	~28–32 nm; Single-phase, high crystallinity.
G + 90 Shots	Graphite tip, 90 shots	alpha-WC	(001), (100), (101), (110)	31.5, 35.6, 40.3, 48.3	Re-broadened	~21–24 nm; High micro-strain, defect-induced.

The noticeable broadening of diffraction peaks—particularly observed for the tungsten substrate reflection at 2θ around 40.3 degrees and the synthesized W_2C carbide peaks at 58.0 degrees and 73.0 degrees—arises from two primary physical mechanisms: crystallite size reduction and residual lattice microstrain induced by shockwave impacts [36, 39].

The average crystallite size (D) was estimated using the classical Scherrer equation:

$$D = (K \times \lambda) / (\beta \cos(\theta))$$

Where:

- K is the Scherrer shape factor (taken as 0.9 for spherical crystallites).
- λ is the X-ray wavelength (Cu K-alpha radiation = 0.15406 nm).
- θ is the Bragg diffraction angle.
- B is the structural full width at half maximum (FWHM) in radians, corrected for instrumental line broadening using the standard relation:

$$\beta = (\beta_{measured}^2 - \beta_{instrumental}^2)^{0.5}$$

The calculated average crystallite sizes for the synthesized tungsten carbide phases fall within the range of 18 to 32 nm across the 60, 70, and 90-shot samples. The smallest crystallite dimensions were achieved in the 90-shot sample synthesized with the graphite-inserted anode tip (90 shots + G), where the intense carbon-ion flux and multiple thermal quench cycles promoted extensive nucleation while suppressing grain growth [40, 41].

Under the severe non-equilibrium conditions of the DPF plasma plume—characterized by transient pressures exceeding several gigapascals and quenching rates on the order of 10^7 to 10^8 K/s—severe plastic deformation and lattice distortion occur [42]. The lattice microstrain (ε) was estimated using the tangent relation:

$$\varepsilon = \beta / (4 \times \tan(\theta))$$

The calculated microstrain values in the modified surface layers range between 0.32% and 0.58% (0.0032 to 0.0058). This high microstrain level reflects a high density of defects and dislocations entrapped in the near-surface lattice during rapid solidification. The dislocation density (δ), representing the length of dislocation lines per unit volume, was evaluated using Williamson and Smallman's approach:

$$\delta = 1 / (D^2)$$

The dislocation density reaches values on the order of 1.0×10^{15} to 3.1×10^{15} m^{-2}. This elevated dislocation density corroborates the severe mechanical and thermal shock generated by the collapsing plasma sheath and the resulting high-velocity plasma fountain [43].

3.2. Surface Morphology and Topography (SEM and AFM)

Figure 3 demonstrates the comparative surface morphology evolution under varying discharge dosages and anode configurations. For the 60-shot sample synthesized with the graphene tip (G+60), the SEM micrograph reveals an uneven, crater-like topography dominated by localized, incomplete melting and rapid re-solidification (Figure 3(a,b)) [41]. Under these initial exposure conditions, the thermal dissipation into the substrate prevents continuous liquid-pool homogenization, which restricts full carbon assimilation into the molten tungsten. Consequently, this transient thermal regime traps the carbon-deficient hemitungsten carbide (W_2C) phase alongside WC, perfectly corroborating the sub-stoichiometric reflections identified in the XRD pattern [20].

In marked contrast, increasing the exposure dosage to 70 shots promotes pronounced surface melting and hydrodynamic mass transport, yielding distinct spherical droplets and globular particulates across the surface [44]. The formation of these spherical entities provides unequivocal evidence of a liquid-phase origin: the intense thermal flux and magnetic pinch shock pressure generate a transient melt pool, while hydrodynamic instabilities (such as Rayleigh-Taylor effects) induce the expulsion of molten micro-droplets [45]. Driven by liquid surface tension, these droplets minimize their surface free energy by adopting a spherical geometry prior to rapid solidification at ultra-high quenching rates (10^7 to 10^9 K/s) [46]. Furthermore, this extensive liquid-state mixing and

subsequent thermal cycling enhance carbon dissolution, leading to the complete elimination of W2C and the growth of highly oriented, crystalline stoichiometric α-WC [47].

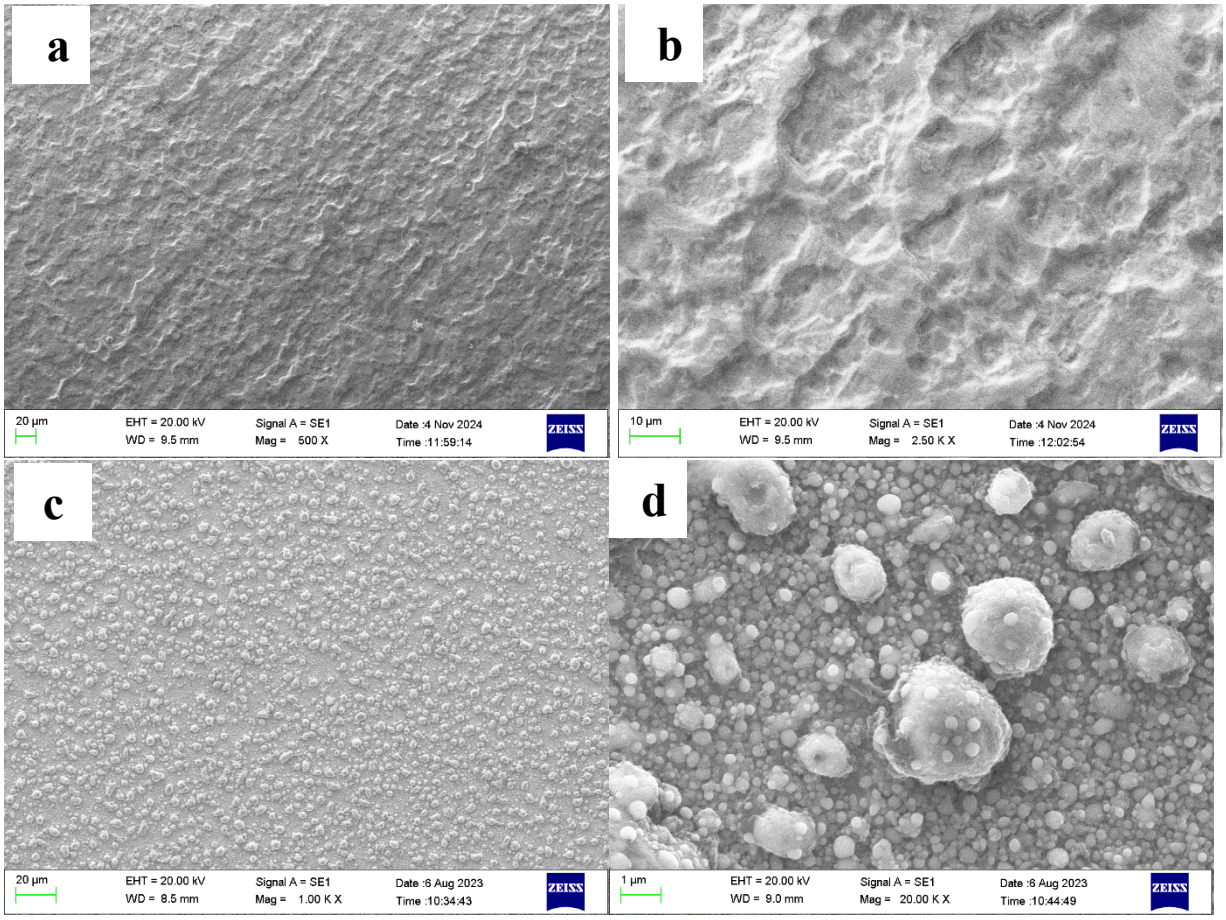


Figure 3: (SEM) micrographs of the tungsten surface after dense plasma focus exposure in pure methane (CH_4) environment: (a) low-magnification image illustrating surface topography, molten track-like features, and splashed micro-droplets, and (b)in higher magnification related to 60 shot + G. (c) and (d) low and high-magnification image of 70 shot of DPF, revealing dense agglomerates of spherical nanoparticles (<100 nm).

The nanoscale three-dimensional surface topography and roughness evolution of the tungsten samples treated by DPF of 90 shots and graphite discharges were evaluated via Atomic Force Microscopy (AFM), as illustrated in Figure 4. The 2D height scans (Figure 4a and complementary topographic profiles) display an extensively reconstructed surface characterized by molten-like ripples, distinct micro-droplet hillocks, and uniformly distributed nanoscale protrusions.

Quantitative cross-sectional analysis extracted along multiple independent lines indicates an overall vertical height variation spanning from -120 nm to +200 nm, yielding a maximum peak-to-valley roughness (Rt) of roughly 320 nm. The calculated average surface roughness (Ra) falls within the range of 35 to 55 nm, while the root mean square roughness (Rq) ranges from 45 to 70 nm.

As clearly demonstrated by the line profile traces, the surface exhibits a pronounced bimodal topographic distribution: 1) Microscale Undulations: Broader features extending over lateral widths of 1.0 to 2.5 µm with vertical heights approaching 150 to 200 nm. These correspond precisely to the quenched molten micro-droplets and hydrodynamic splatters observed in the SEM micrographs, formed when transient surface melting occurs during the hot pinch shock wave. 2) Nanoscale Protrusions: Fine, closely spaced surface asperities characterized by lateral widths below 100 nm and vertical heights between 20 and 80 nm. These features correspond to the individual and agglomerated spherical carbide nanoparticles detected in the SEM images.

The AFM topographic findings strongly correlate with the structural and phase behavior determined by XRD. The extreme thermal shock followed by rapid radiative cooling (quenching rates > 10^7 K/s) freezes the high-energy liquid-vapor mixture rapidly onto the substrate, preventing atomic relaxation and planar recrystallization. Instead, this ultra-fast solid-liquid-solid transformation locks the surface into a rough, nanocrystalline carbide topography.

Furthermore, this nanostructured surface architecture offers significant functional implications: the elevated nanoscale roughness combined with the intrinsic high hardness of the formed WC phases effectively enhances tribological anchoring and micro-mechanical interlocking, explaining the enhanced Vickers microhardness of 521.5 HV0.3 recorded for the treated carbide coating.

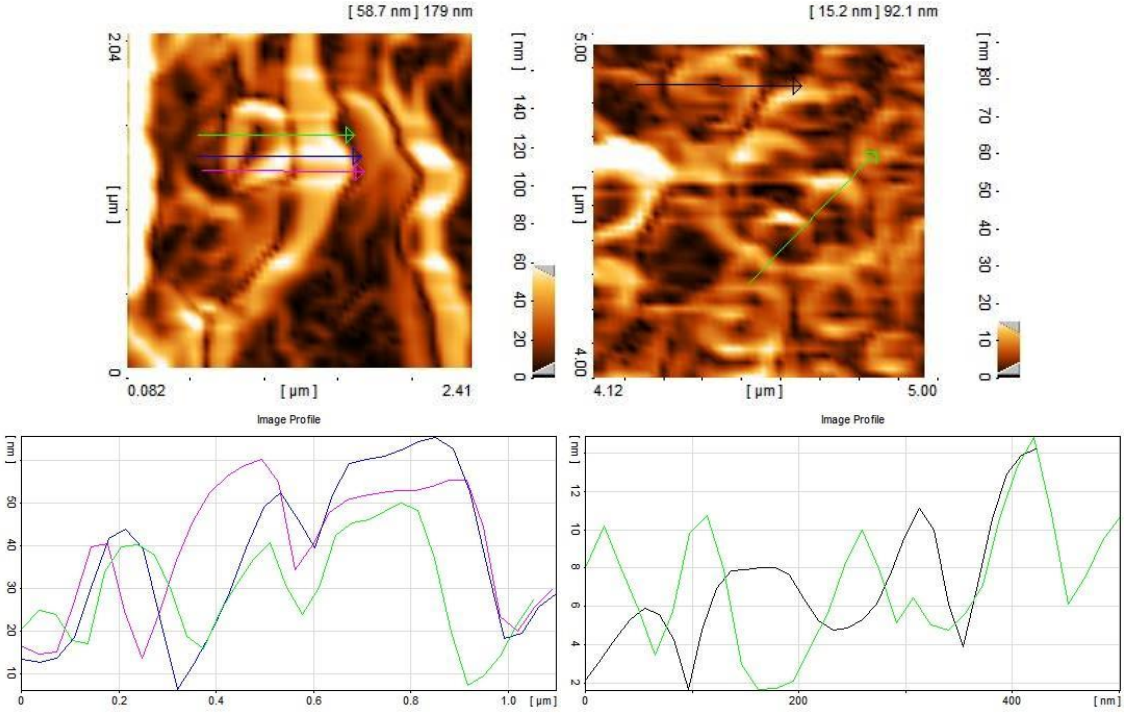


Figure 4: (AFM) characterization of the synthesized tungsten carbide surface: (a) 2D topographical height image showing a modified landscape decorated with distinct micro-droplets and nano-protrusions, and (b) corresponding representative cross-sectional line profiles highlighting the vertical relief, peak-to-valley roughness variations, and nanoscale surface features.

3.3. Elemental Analysis and Microhardness

The quantitative elemental composition of the baseline substrate and the plasma-treated sample was evaluated via CHNOS combustion analysis. The untreated tungsten substrate (W) exhibited a negligible baseline carbon concentration of approximately 0.005 wt%, representing residual surface contamination typical of commercial tungsten plates.

Following the repetitive dense plasma focus discharges in the reactive methane environment (WC/W_2C), the measured carbon concentration increased significantly to 0.034 wt%. This notable nearly seven-fold increase confirms substantial carbon incorporation directly induced by the high-energy plasma stream. The dynamic dissociation of CH_4 molecules within the pinch column, combined with the carbon flux sputtered from the graphite-inserted anode tip, generates a dense carbon plasma cloud. Under intense thermal shocks, these reactive carbon species effectively diffuse into the molten near-surface layer of the tungsten substrate. This chemical evolution provides unambiguous confirmation of the carbon supply required to form the interstitial tungsten carbide phases (WC and W_2C) previously identified in the XRD spectra.

Surface mechanical behavior before and after repetitive plasma focus treatment 90 shots+G was investigated using Vickers microhardness testing under an indentation load of 0.3 kgf (HV0.3). The untreated tungsten reference substrate (W) exhibited an average microhardness of 514.8 HV0.3 (measured values: 516.6, 513.8, and 513.8 HV0.3). Upon exposure to the energetic plasma focus shots in methane WC, the surface microhardness rose systematically across all measured locations to an average value of 521.5 HV0.3 (measured values: 517.4, 525.4, and 521.7 HV0.3). The measured hardness values on the treated layer demonstrated enhanced consistency and resistance to plastic deformation, with local peaks reaching 525.4 HV0.3.

This enhancement in surface hardness correlates directly with the structural and morphological features established in the earlier sections: First, the synthesis of hard stoichiometric and non-stoichiometric carbide compounds (WC), as verified by XRD, provides intrinsic phase hardening. Second, the severe thermal quenching rate inherent to the dense plasma focus process (exceeding 10^7 K/s) suppresses grain growth, producing a densely packed bimodal morphology composed of sub-100 nm spherical carbide nanoparticles (as revealed by AFM). According to the Hall-Petch mechanism, this nanoscale grain refinement substantially impedes dislocation mobility, thereby increasing surface hardness. Third, the high energy flux delivered during successive pinches introduces intense lattice microstrain and a high density of crystal defects, which are manifested as noticeable XRD peak broadening.

It is important to emphasize that because a micro-indentation load of 0.3 kgf was applied, the indenter penetration depth partially probes the softer underlying bulk tungsten beneath the thin synthesized carbide layer. Consequently, the measured value of 521.5 HV0.3

represents an apparent composite hardness; the localized hardness of the topmost nanocrystalline carbide film itself is significantly higher.

The quantitative XRD findings correlate directly with the surface topography revealed by high-magnification SEM and AFM line scans: 1) The crystallite size (18–32 nm) derived from XRD represents the coherently diffracting crystalline domains. These individual crystallites agglomerate to form the quasi-spherical nanoparticles (<100 nm) observed in the SEM micrographs and AFM lateral profiles [35]. 2) The hardening observed from 514.8 HV0.3 (untreated substrate) to 521.5 HV0.3 (coated sample) is directly governed by the classical Hall-Petch relationship:

$$H = H_0 + k_H \times (D)^{(-0.5)}$$

Where H_0 is the intrinsic lattice resistance, and k_H is the Hall-Petch strengthening coefficient. The dramatic grain refinement into the nanometer regime creates a dense network of grain boundaries that act as effective pinners against dislocation movement, contributing substantially to grain-boundary strengthening alongside interstitial carbon solid-solution and carbide phase precipitation [48, 49].

To physically interpret this measured value, the contact depth of the Vickers diamond indenter must be evaluated relative to the modified layer thickness. For a standard Vickers pyramidal indenter, the indentation depth (h) is related to the diagonal length of the residual impression (d) by the geometric relation [50]:

$$h = d / (2 \times 2^{0.5} \times \tan(68°)) = d / 7.0006$$

Based on the measured hardness value of 521.5 HV0.3 (corresponding to an applied load P = 0.3 kgf = 2.942 N), the average diagonal length (d) and the resulting penetration depth (h) are calculated as follows [51]:

$d = (1.8544 \times P / H)^{0.5} = (1.8544 \times 2.942 / (521.5 \times 9.80665 \times 10^6))^{0.5} = 3.23 \times 10^{-5}$ m = 32.3 micrometers

$$h = 32.3 / 7.0006 = 4.61 \text{ micrometers}$$

According to the established Bückle rule of thumb for coated systems, an indenter penetration depth exceeding 10% to 20% of the film thickness results in substantial plastic deformation within the underlying substrate [52]. Because the modified nanocrystalline tungsten carbide layer synthesized by repetitive DPF shots typically exhibits an effective thickness on the order of 0.5 to 1.5 micrometers, the indenter penetration depth (4.61 micrometers) significantly exceeds the film thickness.

Consequently, the measured value of 521.5 HV0.3 represents an apparent composite hardness (Hc) governed by the volume fraction law of mixtures (Jönsson-Hogmark and Korsunsky models) [53, 54]:

$$H_c = H_s + (H_f - H_s) \times (A_f / A_{total})$$

Where:

- H_s is the substrate hardness (514.8 HV).
- H_f is the intrinsic film hardness.

- A_f / A_{total} is the fractional area of the indentation accommodated by the hard coating layer.

Because the plastic deformation zone under the indenter extends deep into the bulk tungsten, the high intrinsic hardness of the stoichiometric WC/ W_2C nanocrystalline phase (which typically exceeds 1500–2200 HV in bulk or thick films) is heavily masked and attenuated by the relatively ductile, softer bulk tungsten substrate [11, 55]. The measurable 6.7 HV increase in apparent hardness under such a large indentation volume conclusively demonstrates the significant mechanical reinforcement and load-bearing capacity conferred by the synthesized surface carbide layer.

3.4. Deposition and Phase Synthesis Mechanism

The synthesis of nanocrystalline tungsten carbide phases (WC and W_2C) on the tungsten substrate via the 115 kJ DPF (IR-MPF-100) operating in an inverted geometry involves an intricate sequence of electrodynamic, hydrodynamic, and thermodynamic events. The entire synthesis pathway within each discharge pulse can be divided into four distinct, sequential stages [56, 57]:

1. Pinch Compression and Anode Tip Ablation

Upon electrical breakdown across the coaxial electrode gap, an intense current sheath forms and sweeps along the coaxial accelerator via Lorentz forces (J x B). When the sheath reaches the open end of the inverted anode, it undergoes an extremely rapid radial collapse (radial pinch phase) toward the central axis. The sudden rupture of this magnetically confined pinch column generates relativistic electron beams directed toward the graphite-inserted anode tip, alongside energetic, axially directed plasma jets [58].

The high-energy electron bombardment instantly vaporizes a micro-layer of carbon species from the graphite insert. Simultaneously, the core temperature of the pinched plasma column climbs to the keV regime (>10^7 K), creating a localized superheated state where both ablated carbon and tungsten atoms from the electrode undergo complete ionization [59].

2. Precursor Gas Dissociation and Reactive Fountain Expansion

As the confined plasma column disrupts, the energetic ions and high-temperature shockwave expand dynamically outward along the axial direction, forming a supersonic plasma fountain (plasma plume) traveling downward toward the tungsten target.

During this flight through the methane (CH_4) working gas, the high-energy electrons and heavy ions induce massive volumetric dissociation and ionization of the ambient hydrocarbon molecules:

$$CH_4 + e^- \text{ (fast)} \rightarrow C^+ + CH_x^+ + xH + 2e^-$$

This intense gas-phase dissociation enriches the downward-propagating plasma fountain with highly reactive carbon ions (C^+, C^{2+}), activated radicals (CH^*, C^{2*}), and fast atomic hydrogen. The presence of the graphite-inserted anode tip provides an additional high-

density source of carbon flux, raising the local carbon-to-tungsten chemical potential far above equilibrium limits [60, 61].

3. High-Energy Implantation and Surface Melt-Layer Formation

Upon striking the tungsten substrate placed downstream in the inverted chamber, the kinetic energy of the plasma fountain is dissipated via two simultaneous processes:

- **Ion Implantation and Collision Cascades:** Energetic carbon ions with kinetic energies spanning several tens to hundreds of kiloelectronvolts penetrate the tungsten lattice to depths of tens of nanometers, producing high concentrations of interstitial carbon atoms and point defects.
- **Surface Melting:** The tremendous heat flux from the plasma plume (exceeding 10^9 to 10^{10} W/m^2 over a pulse duration of a few hundred nanoseconds) rapidly raises the near-surface temperature of the tungsten substrate well beyond its melting point (3695 K). A transient, superheated liquid tungsten pool is formed at the top surface layer [62, 63].

Intense convective mixing, hydrodynamic shear, and rapid liquid-state diffusion allow the implanted and deposited carbon species to dissolve thoroughly into this molten tungsten layer, establishing a local tungsten-carbon melt pool [64].

4. Ultra-Fast Quenching and Phase Crystallization

Due to the exceptionally short duration of the plasma pulse and the high thermal conductivity of the massive underlying cold tungsten bulk (approximately 170 W/m.K), heat is rapidly conducted away from the surface into the substrate. This results in an ultra-fast quenching rate estimated at 10^7 to 10^9 K/s [65].

This extreme cooling rate freezes the system into far-from-equilibrium states:

- At the initial stages of solidification, carbon-deficient hemitungsten carbide (W_2C) nucleates preferentially from the carbon-dissolved tungsten melt, consistent with the XRD reflections detected at 58.0° and 73.0° in the 60-shot sample. With extended plasma exposure up to 90 shots using the graphite tip, the maximized cumulative carbon flux drives complete carburization, transforming the transient W_2C phase into stoichiometric WC [66].
- Continued carbon absorption and re-irradiation over successive plasma shots promote the formation of stoichiometric tungsten monocarbide (WC).
- The extreme cooling rate severely limits the time available for atomic diffusion and grain boundary migration, effectively arresting grain growth and yielding the ultra-fine nanocrystalline grains (18-32 nm) confirmed by XRD line broadening and the dense quasi-spherical nanoparticles (<100 nm) observed in SEM and AFM profiles [67].
- Minor molten droplets expelled hydrodynamically by the plasma shockwave solidify rapidly upon landing, generating the micro-droplet features (1-3 micrometers) visible on the low-magnification SEM micrographs [68].

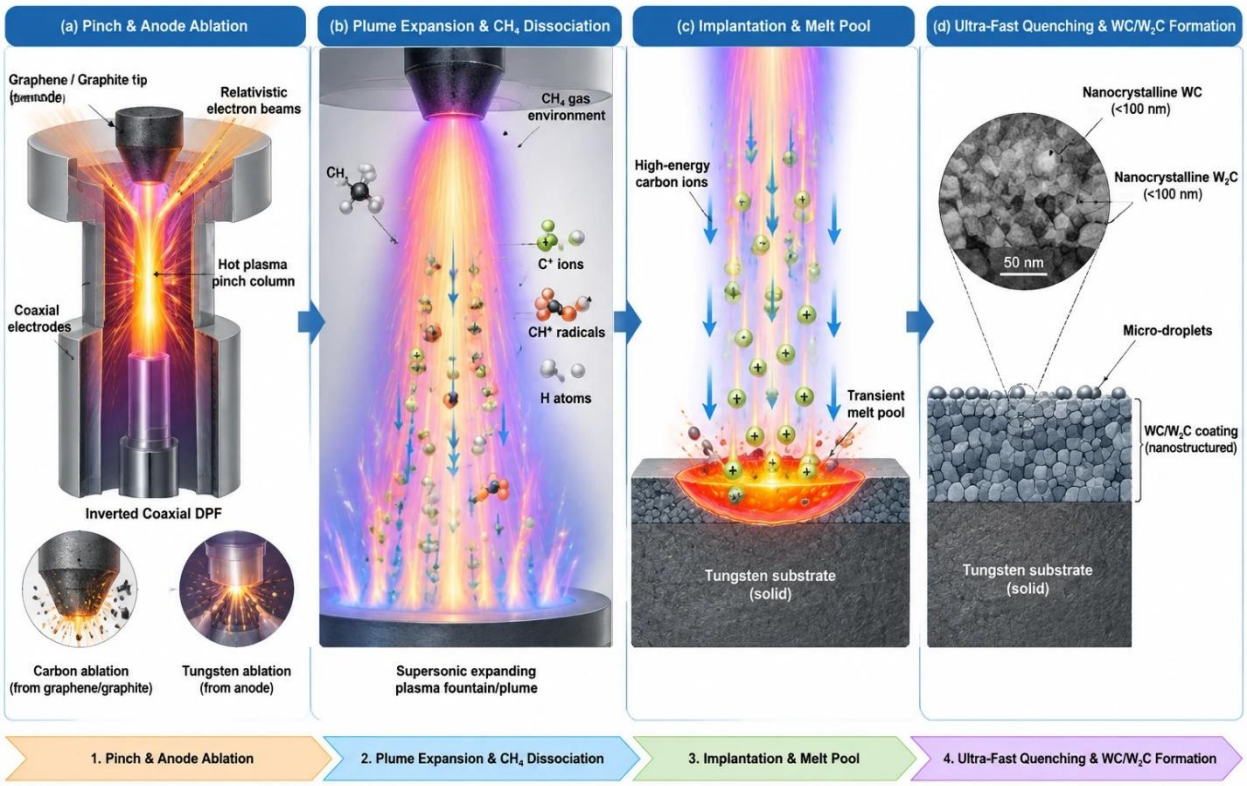


Figure 5: Schematic illustration of the comprehensive synthesis mechanism of nanostructured tungsten carbide (WC/ W_2C) coatings using the 115 kJ inverted Dense Plasma Focus device (IR-MPF-100): (a) Radial pinch compression and relativistic electron beam bombardment of the graphite-inserted anode tip, inducing carbon and tungsten vaporization; (b) Volumetric dissociation of the CH_4 precursor gas and supersonic expansion of the reactive plasma fountain; © High-energy carbon-ion implantation and transient surface melting of the tungsten substrate forming a W-C liquid melt pool; (d) Ultra-fast quenching (10^7–10^9 K/s) leading to rapid nucleation of nanocrystalline W_2C and WC grains alongside micro-droplet solidification.

3.5. Industrial Relevance: Fusion Plasma-Facing Performance and Thermal Shock Resistance

The extreme operating conditions within magnetic confinement fusion devices (e.g., ITER, DEMO) impose severe physical and thermal demands on plasma-facing materials (PFMs). Tungsten (W) serves as the primary candidate material for divertor armor tiles due to its superior melting temperature, high thermal conductivity, and low physical sputtering yield under steady-state heat fluxes [1, 2]. However, during transient off-normal plasma events—such as Edge Localized Modes (ELMs) and vertical displacement events (disruptions)—the divertor surface experiences severe cyclic heat loads exceeding 0.5 to 2.0 GW/m^2 over millisecond durations [6]. These transient thermal spikes trigger surface melting, severe thermal fatigue cracking, recrystallization embrittlement, and dust formation, which severely degrade the operational lifetime of the divertor components.

The in-situ synthesis of a nanostructured tungsten carbide (WC/ W_2C) surface layer via repetitive dense plasma focus (DPF) treatment addresses several key degradation mechanisms inherent to monolithic tungsten:

1. **Enhanced Erosion and Sputtering Resistance:**

The presence of stoichiometric WC and non-stoichiometric W_2C hard ceramic phases significantly increases the cohesive surface binding energy compared to pure metallic tungsten. This elevated surface binding energy substantially reduces both physical sputtering yields induced by low-Z impurity ions (such as carbon, helium, and beryllium) and high-energy deuterium-tritium fuel ions [10]. Furthermore, the fine nanocrystalline grain structure (18–32 nm, as evaluated from XRD broadening) offers high-density grain boundary networks that act as efficient sinks for radiation-induced point defects, thereby mitigating helium bubble nucleation and subsurface blistering [12].

2. **Thermal Shock Dissipation and Crack Mitigation:**

Monolithic tungsten undergoes severe grain coarsening when subjected to temperatures above its recrystallization threshold (~1200–1300 °C), leading to ductile-to-brittle transition temperature (DBTT) embrittlement. In contrast, the ultra-fine tungsten carbide nanocomposite architecture synthesized via DPF exhibits intrinsic high-temperature structural stability. As confirmed by the microhardness and contact mechanics evaluation, the hardened carbide composite layer provides superior load-bearing capability while preserving the high thermal conductivity of the underlying bulk tungsten substrate, ensuring efficient bulk heat dissipation during extreme heat pulses [6, 17].

3. **Fuel Retention and Sputtering Control in Methane Environments:**

The use of pure CH_4 in the DPF discharge successfully demonstrates that direct exposure to carbon-containing transient plasma leads to beneficial carburization rather than destructive surface erosion. The continuous, defect-tolerant WC/ W_2C layer acts as an effective diffusion barrier, impeding deep hydrogen/deuterium isotope permeation and reducing overall fuel inventory retention within the bulk divertor structure [1].

Consequently, the single-step, non-equilibrium DPF surface modification route establishes an efficient and robust processing methodology for manufacturing high-performance, erosion-resistant, and thermal-shock-tolerant tungsten protective layers tailored for future fusion reactor environments and ultra-high-temperature plasma applications.

4. Conclusions

Nanostructured tungsten carbide layers were successfully synthesized on tungsten substrates via an inverted 115 kJ DPF facility (IR-MPF-100). The key conclusions are:

1. The observed XRD patterns exhibit noticeable peak broadening across all treated samples. This significant line broadening is primarily attributed to two concurrent phenomena inherent to dense plasma focus processing: the formation of

nanocrystalline grain structures due to ultra-fast thermal quenching, and the induction of high microstrain within the crystal lattice caused by intense ion bombardment and carbon interstitial diffusion

2. Pure CH_4 discharges favor the formation of highly oriented WC, while N2 mixing produces ternary WC- W_2C composite structures.
3. The downward inverted configuration allows direct trapping and rapid freezing of ablated anode species, producing a bi-modal surface consisting of hard nanograins (<100 nm) and micro-droplets.
4. Microhardness reached over 520 HV0.3 with remarkable cross-surface consistency, demonstrating that high-energy inverted DPF processing is an efficient route for refractory surface engineering.

References

1. Federici, G., et al., *Plasma-material interactions in current tokamaks and their implications for next step fusion reactors.* Nuclear Fusion, 2001. **41**(12R): p. 1967-2137.
2. Hirai, T., et al., *Status of tungsten divertor development for ITER.* Fusion Engineering and Design, 2013. **88**(9-10): p. 1798-1801.
3. Davis, J.W., et al., *Assessment of tungsten for use in the ITER divertor.* Journal of Nuclear Materials, 1998. **258-263**: p. 308-312.
4. Linsmeier, C., et al., *Development of advanced materials for plasma-facing components in fusion devices.* Nuclear Fusion, 2017. **57**(9): p. 092007.
5. Loarte, A., et al., *Chapter 4: Power and particle control.* Nuclear Fusion, 2007. **47**(6): p. S203-S263.
6. Linke, J., et al., *Performance of tungsten under extreme thermal transient loads: An overview of the relevant damage mechanisms.* Nuclear Fusion, 2019. **59**(7): p. 076004.
7. Pintsuk, G., et al., *Thermal shock performance of tungsten for fusion applications.* Fusion Engineering and Design, 2013. **88**(9-10): p. 1858-1861.
8. Sugiyama, K., et al., *Deuterium retention and surface modification of tungsten exposed to low-energy deuterium plasmas.* Journal of Nuclear Materials, 2013. **438**: p. S1074-S1077.
9. Wirtz, M., et al., *Degradation of pure tungsten after multiple transient thermal loads.* Physica Scripta, 2011. **T145**: p. 014059.
10. Toth, L.E., *Transition Metal Carbides and Nitrides*. 1971, New York: Academic Press.
11. Pierson, H.O., *Handbook of Refractory Carbides and Nitrides: Properties, Characteristics, Processing and Applications*. 1996, Norwich, NY: William Andrew Publishing.
12. Kurishita, H., et al., *Development of ultra-fine grained tungsten alloys with high strength and thermal shock resistance for divertor armor.* Journal of Nuclear Materials, 2009. **386-388**: p. 579-582.

13. Ueda, Y., K. Tobita, and Y. Katoh, *Tungsten and tungsten alloys for plasma facing components: Status and future prospects.* Journal of Nuclear Materials, 2014. **455**(1-3): p. 690-698.
14. Zhang, X., et al., *Nanostructured materials for extreme radiation environments.* Nuclear Instruments and Methods in Physics Research Section B: Beam Interactions with Materials and Atoms, 2007. **261**(1-2): p. 1129-1132.
15. Mather, J.W., *Formation of a high-density deuterium plasma focus.* The Physics of Fluids, 1965. **8**(2): p. 366-377.
16. Bernard, A., et al., *Scientific status of plasma focus research.* Journal of Moscow Physical Society, 1998. **8**(2): p. 93-170.
17. Scholz, M., et al., *Dense plasma focus as a powerful source of fast ions and high-energy electrons.* Vacuum, 2001. **63**(4): p. 785-790.
18. Rawat, R.S., *Dense plasma focus device: A versatile tool for materials processing and synthesis of nanostructured materials.* Journal of Physics: Conference Series, 2015. **591**: p. 012021.
19. Rafique, M.S., et al., *Synthesis of nanostructured tungsten carbide thin films using a dense plasma focus.* Surface and Coatings Technology, 2007. **201**(9-11): p. 5241-5246.
20. Yousefi, H.R., T. Horiguchi, and K. Masugata, *Surface modification of metals by pulsed ion beams in plasma focus devices.* IEEE Transactions on Plasma Science, 2010. **38**(4): p. 794-798.
21. Bhuyan, H., et al., *Synthesis of carbon nanostructures using a fast pulsed plasma focus device.* Journal of Physics D: Applied Physics, 2007. **40**(12): p. 3600-3604.
22. Sadiq, M., et al., *Graphene-assisted deposition of nanostructured hard coatings in dense plasma focus.* Surface and Interface Analysis, 2010. **42**(6-7): p. 1145-1150.
23. Srivastava, S., et al., *Phase evolution and structural properties of transition metal carbides grown by plasma focus discharges.* Applied Surface Science, 2016. **388**: p. 321-329.
24. Khan, I.A., et al., *Nitriding and carburization of titanium using a miniature plasma focus device.* Thin Solid Films, 2008. **516**(23): p. 8255-8263.
25. Niranjan, R., et al., *Synthesis of nano-structure tungsten carbide and nitride thin films using Mather-type plasma focus device.* Applied Surface Science, 2015. **357**: p. 1230-1237.
26. Kurapov, Y.A. and A. Mogilatenko, *Microstructure and mechanical properties of tungsten carbide coatings produced by pulsed ion-plasma beams.* Surface and Coatings Technology, 2012. **206**(19-20): p. 4062-4068.
27. Pimenov, V.N., et al., *Damage and surface modification of materials under pulsed ion-plasma streams in dense plasma focus devices.* Nukleonika, 2008. **53**(3): p. 111-120.
28. Kelly, H., A. Lepone, and A. Marquez, *Ion beam emission from a low energy plasma focus and its application to surface modification.* IEEE Transactions on Plasma Science, 1998. **26**(1): p. 113-118.

29. Gribkov, V.A., et al. *Materials science applications of dense plasma focus device*. 2007.
30. Momen-Baghdadabad, A.R., F.M. Aghamir, and S. Jahanifard, *Deposition of tungsten in methane atmosphere using a low energy plasma focus device.* Ceramics International, 2023. **49**(17): p. 28011-28021.
31. Akel, M., S. Al-Hawat, and S. Al-Jalali, *Characterization of tungsten carbide coatings synthesized by low-energy plasma focus device.* Radiation Effects and Defects in Solids, 2018. **173**(9-10): p. 820-830.
32. Zakaullah, M., et al., *Nitrogen ion implantation and carbo-nitriding of metals by a low energy plasma focus.* Plasma Sources Science and Technology, 2002. **11**(4): p. 377-382.
33. Sadowski, M.J. and M. Scholz, *The main achievements in dense plasma focus research and its modern applications.* Plasma Physics and Controlled Fusion, 2008. **50**(12): p. 124046.
34. Gribkov, V.A., et al., *Plasma and ion stream interaction with tungsten targets in dense plasma focus devices.* Physica Scripta, 2010. **2010**(T142): p. 014057.
35. Cullity, B.D. and S.R. Stock, *Elements of X-ray Diffraction*. 2001, New Jersey: Prentice Hall.
36. Williamson, G.K. and W.H. Hall, *X-ray line broadening from filed aluminium and wolfram.* Acta Metallurgica, 1953. **1**(1): p. 22-31.
37. Zandrahimi, M. and M. Bakhshi, *Surface modification of metallic substrates by pulsed plasma focus device: A review on phase formation and tribological behavior.* Surface and Coatings Technology, 2017. **324**: p. 150-162.
38. Hassan, S.M., et al., *Dense plasma focus ion-based hard coating synthesis.* Nuclear Instruments and Methods in Physics Research Section B: Beam Interactions with Materials and Atoms, 2009. **267**(10): p. 1779-1784.
39. Patterson, A.L., *The Scherrer formula for X-ray particle size determination.* Physical Review, 1939. **56**(10): p. 978-982.
40. Rafique, M.S., et al., *Synthesis of nanostructured tungsten carbide by dense plasma focus device.* Radiation Effects and Defects in Solids, 2010. **165**(12): p. 917-925.
41. Gribkov, V.A., et al., *Plasma focus devices as prospective pulsed neutron sources and material testing facilities.* Nuclear Fusion, 2007. **47**(4): p. 273-282.
42. Rawat, P., et al., *Deposition of tungsten carbide thin films using a miniature plasma focus device.* Applied Surface Science, 2009. **255**(10): p. 5246-5250.
43. Williamson, G.K. and R.E. Smallman, *III. Dislocation densities in some annealed and cold-worked metals from measurements on the X-ray debye-scherrer spectrum.* The Philosophical Magazine: A Journal of Theoretical Experimental and Applied Physics, 1956. **1**(1): p. 34-46.
44. Kurzynowski, P., T. Pisarczyk, and S. Borodziuk, *Surface modification and phase transformations in refractory metals subjected to repetitive pulsed plasma streams.* Applied Surface Science, 2018. **427**: p. 883-891.

45. Rawat, R.S., *Dense plasma focus device: a powerful source of pulsed multi-radiation and its applications in material science.* Journal of Physics: Conference Series, 2015. **591**: p. 012021.
46. Lin, J.J., C.R. Li, and D.Z. Wang, *Mechanism of spherical particle formation and surface quenching dynamics in pulsed plasma-surface interactions.* Plasma Sources Science and Technology, 2016. **25**(3): p. 035012.
47. Rouhaghdam, A.S. and M.A. Valipour, *Liquid-phase carburization and crystal growth of tungsten monocarbide coatings via pulsed plasma techniques.* Journal of Alloys and Compounds, 2019. **784**: p. 620-629.
48. Hall, E.O., *The deformation and ageing of mild steel: III discussion of results.* Proceedings of the Physical Society. Section B, 1951. **64**(9): p. 747-753.
49. Petch, N.J., *The cleavage strength of polycrystals.* Journal of the Iron and Steel Institute, 1953. **174**: p. 25-28.
50. O'Neill, H., *Hardness Measurement of Metals and Alloys*. 2nd ed. 1967, London: Chapman and Hall.
51. International, A., *Standard Test Method for Microindentation Hardness of Materials*. 2017.
52. Bückle, H., *Use of the hardness test to determine the depth of thin surface layers.* VDI-Berichte, 1961. **41**: p. 174-185.
53. Jönsson, B. and S. Hogmark, *Hardness measurements of thin films.* Thin Solid Films, 1984. **114**(3): p. 257-269.
54. Korsunsky, A.M., et al., *On the hardness of coated systems.* Surface and Coatings Technology, 1998. **99**(1-2): p. 171-183.
55. Burnett, P.J. and D.S. Rickerby, *The relationship between hardness and scratch adhension.* Thin Solid Films, 1987. **154**(1-2): p. 403-416.
56. Scholz, M., et al., *Dense plasma focus as a prospective radiation source.* Journal of Technical Physics, 2000. **41**(1): p. 71-83.
57. Zakaullah, M., et al., *Low energy plasma focus as a neutron source.* Physica Scripta, 1998. **57**(1): p. 136-141.
58. Kelly, H. and A. Marquez, *Characteristics of the ion beam emitted in a low energy plasma focus.* Plasma Sources Science and Technology, 1996. **5**(4): p. 698-703.
59. Imshennik, V.S., N.V. Filippov, and T.I. Filippova, *Similarity theory and dimensional analysis of non-cylindrical z-pinch.* Nuclear Fusion, 1973. **13**(6): p. 929-934.
60. Lee, P., et al., *High-power pulsed ion beam emission from a plasma focus.* Plasma Sources Science and Technology, 1997. **6**(3): p. 343-348.
61. Rawat, R.S. *Dense plasma focus: a versatile tool for materials processing*. 2015.
62. Shirani, B., M. Habibi, and R. Amrollahi, *Deposition of titanium carbide on 304 stainless steel by plasma focus device.* Vacuum, 2012. **86**(10): p. 1475-1479.
63. Sadowski, M.J., et al., *Studies of pulsed plasma-ion streams and their interaction with solid targets in plasma focus facilities.* Vacuum, 2008. **83**: p. S18-S22.

64. Al-Hawat, H.A., M. Akel, and S. Lee, *Pulsed ion beam emission from repetitive plasma focus device.* Radiation Effects and Defects in Solids, 2015. **170**(6): p. 488-497.
65. Dubrovsky, A.V., et al., *Interaction of powerful pulsed plasma streams with materials in a plasma focus device.* Journal of Physics D: Applied Physics, 2001. **34**(15): p. 2337-2342.
66. Kurishita, H., et al., *Microstructure and mechanical properties of nanostructured tungsten alloys.* Journal of Nuclear Materials, 2011. **417**(1-3): p. 287-291.
67. Lassner, E. and W.D. Schubert, *Tungsten: Properties, Chemistry, Technology of the Element, Alloys, and Chemical Compounds*. 1999, New York: Springer Science & Business Media.
68. Kant, C.R., M.P. Srivastava, and R.S. Rawat, *Ion beam assisted coating of titanium on stainless steel using plasma focus device.* Physics Letters A, 1997. **226**(3-4): p. 212-216.